Comparison of the Magnetic and Optical Properties of Wide-Gap (II,Mn)VI Nanostructures Confined in Mesoporous Silica

Felix J. Brieler,[a] Petra Grundmann,[a] Michael Fröba,*[a] Limei Chen,[b] Peter J. Klar,*[b] Wolfram Heimbrodt,[b] Hans-Albrecht Krug von Nidda,[c] Thomas Kurz,[c] and Alois Loidl[c]

Keywords: Mesoporous materials / Diluted magnetic semiconductors / Host–guest systems / Nanostructures / $Cd_{1-x}Mn_xS$ / $Cd_{1-x}Mn_xSe$ / $Zn_{1-x}Mn_xS$

Arrays of highly ordered $Cd_{1-x}Mn_xSe$, $Cd_{1-x}Mn_xS$, and $Zn_{1-x}Mn_xS$ nanoparticles with x ranging from 0.01 to 0.3 and with lateral dimensions of 3, 6, and 9 nm were synthesised within mesoporous SiO_2 host structures of the MCM-41 and SBA-15 type. The hexagonal symmetry of these arrays (space group *p*6*m*) and the high degree of order were confirmed by X-ray diffraction and transmission electron microscope studies. Physisorption measurements show the progressive filling of the pores of the SiO_2 host structures, while photoluminescence excitation (PLE) and electron paramagnetic resonance (EPR) studies confirm the good crystalline quality of the incorporated (II,Mn)VI guest species. The effects of the reduction of the lateral dimensions on the electronic properties of the diluted magnetic semiconductor were studied by PLE spectroscopy. Due to the quantum confinement of the excitons in the nanostructures an increase of the direct band gap with decreasing particle size is observed. The magnitude of the confinement effects increases with increasing excitonic Bohr radius of the (II,Mn)VI, i.e. it is largest for (Cd,Mn)Se and smallest for (Zn,Mn)S. Moreover, an increased band-gap bowing with Mn content is observed for the Cd compounds and can be correlated with the modification of the magnetic properties. Surprisingly, no band-gap bowing with x is observed for the $Zn_{1-x}Mn_xS$ nanostructures. Analysis of the EPR linewidth and EPR intensity show that macroscopic magnetic properties such as the Curie–Weiss temperature are affected by the reduction of the lateral dimensions. The microscopic coupling between the Mn ions (e.g. the exchange constants J_{nn} and J_{nnn}) is not altered to a first approximation.

1. Introduction

The fabrication of ordered assemblies of particles on the nanometre scale is a challenge in material science, which has become more and more important over the last decades. With the availability of highly ordered arrays of particles well defined in size in the range of a few nanometres only, the understanding of the unusual dependence of electronic, optical and magnetic properties on size and shape of those nanoparticles has increased significantly. Most of the procedures to obtain 2D magnetic semiconductor nanostructures, i.e. quantum wells, require nonequilibrium growth conditions, which can be realised, for example, by molecular beam epitaxy (MBE) under ultra high vacuum or metal-organic vapour-phase epitaxy (MOVPE). In order to fabricate 0D quantum dots or 1D quantum wires, the conventionally used top-down approach (see Figure 1) is to start with two-dimensional quantum wells and to use a lithographic pattern definition followed by a pattern transfer, usually a subsequent etching procedure[1–7] or a controlled local diffusion process due to ion-bombardment.[8,9] Such top-down approaches usually only yield magnetic semiconductor nanostructures of good structural and optical quality for lateral sizes larger than about 50 nm. Below this size, fabrication-induced surface damage deteriorates the quality of the structures and has a strong undesired effect on optical and magnetic properties. This makes it difficult to separate intrinsic and extrinsic properties in a study of the electronic and magnetic properties as a function of lateral size of the nanostructure.

[a] Institute of Inorganic and Analytical Chemistry, Justus Liebig University Gießen,
Heinrich-Buff-Ring 58, 35392 Gießen, Germany
E-Mail: michael.froeba@anorg.chemie.uni-giessen.de
[b] Department of Physics and Material Sciences Center, Philipps University of Marburg,
Renthof 5, 35032 Marburg, Germany
E-Mail: klarp@mailer.uni-marburg.de
[c] Experimental Physics V, Electronic Correlations and Magnetism, Institute of Physics, University of Augsburg,
Universitätsstraße 2, 86135 Augsburg, Germany

MICROREVIEWS: This feature introduces the readers to the authors' research through a concise overview of the selected topic. Reference to important work from others in the field is included.

Felix J. Brieler is a PhD student in the group of Prof. Fröba in Gießen (Germany). He obtained his diploma in Chemistry on nanostructured semiconductors within mesoporous MCM-41 silica phases in the same group in Hamburg (Germany) in 2000. Since then, he has been working on his PhD thesis "nanostructured diluted magnetic semiconductors within mesoporous silica", which he will finish later this year. He stayed in Exeter (Great Britain) from April to May 1998 as an exchange student.

Petra Grundmann was born in 1961 and started her practical training in 1979 in Dresden (Germany). After completion in 1981 she worked in a research laboratory before she came to the Institute of Inorganic and Analytical Chemistry at the Justus Liebig University in Gießen (Germany) in 1993. She has worked in the group of Prof. Fröba since 2001.

Prof. Dr. Michael Fröba was born in Lübeck (Germany) in 1962 and studied chemistry in Würzburg and Hamburg. He obtained his PhD in 1993 in the group of Prof. Wolfgang Metz at the Institute of Physical Chemistry at the University of Hamburg (Germany). After that he stayed at the Lawrence Livermore National Laboratory (California, USA) from 1994 to 1996. He completed his Habilitation in 2000 at the University of Hamburg in Inorganic Chemistry. From 2000 to 2001 he was appointed associate professor (C3) at the University of Erlangen-Nuremberg (Germany). Since 2001 he is a full professor (C4) in Gießen and head of the Institute of Inorganic and Analytical Chemistry. He is author/coauthor of about 100 scientific publications, including several reviews and book articles. His research interests include porous materials with a focus on the template-directed synthesis and characterisation of mesoporous materials with different morphologies as well as the formation of nanostructures within different porous matrices.

Dr. Limei Chen is currently a researcher at the Physics Department of the Philipps-University of Marburg (Germany). She majored in Chemistry at Beijing Normal University (China) and obtained her BSc and MSc degrees in 1988 and 1991, respectively. In 1992 she obtained a scholarship from the British Council and UK Overseas Development Agency and worked at North East Wales Institute (UK) as a trainee where she obtained the Certificate of British Council Technical Training. From 1994 to 1997 she was the recipient of the first Norwich Research Park Studentship and obtained her PhD degree at the University of East Anglia (UK) in Physics. After a short spell as postdoctoral assistant at the University of East Anglia (UK), she started to work as a postdoctoral researcher at the Philipps-University of Marburg in 1998. Limei Chen is author/coauthor of about 25 scientific publications. Her research interests include magnetic and optical properties of novel nanostructures.

Dr. Peter J. Klar is currently a lecturer of Physics at the Philipps-University of Marburg (Germany). He obtained his Diploma in Physics at the University of Hamburg (Germany) in 1993,and his PhD at the University of East Anglia (UK) in 1997. After two short spells as postdoctoral assistant at the University of East Anglia and at the University of Surrey (UK) he moved on to the Philipps-University of Marburg in 1998. There he completed his Habilitation in Experimental Physics in 2004 and was appointed Privatdozent in 2005. He is author/coauthor of about 90 scientific publications, including several reviews and book articles. His research interests include physics of magnetic semiconductors and hybrids for spintronics, of III-N-V semiconductor structures for opto-electronics, of novel nanostructures ranging from nanomagnetism to applications in catalysis, and material and device characterisation in general.

Prof. Dr. Wolfram Heimbrodt was born 1954 in Berlin, Germany. He received his Diploma in Physics in 1980 from the Technical University of Dresden. He carried out his PhD. thesis in the group of Prof. Otfried Goede at the Humboldt-University of Berlin in 1985 working on the optical properties of isovalent impurities in II-VI semiconductors. Since 1986 he has worked as a postdoctoral Research Fellow in the Institute of Optics and Spectroscopy at the HU-Berlin. In 1993 he became the head of Group Spectroscopy of Semiconductor Microstructures in the Institute of Physics at the HU-Berlin and received his Habilitation in 1996, the main research interest being spintronics and magnetic semiconductors. Between 1996 and 1997 he worked as Senior Research Fellow with Prof. J. J. Davies at the University of East Anglia (UK). In 1997 he became a Professor of Experimental Physics at the Philipps-University Marburg (Germany).

Dr. Hans-Albrecht Krug von Nidda is a scientific employee and academic councillor at the University of Augsburg (Germany). He studied Physics at the Technical University in Darmstadt where he obtained his diploma in 1992. He was a PhD student in the group of Prof. Loidl, working on a project within the "Sonderforschungsbereich 252" (electronically highly correlated metallic compounds), and completed his thesis on electron spin resonance in heavy fermion compounds in 1997. Later, he moved with the group of Prof. Loidl to Augsburg where he is working as a postdoc and is supervisor of a sub group on electron spin resonance. Since 2000, he is the head of the subproject on metal-insulator transitions and order of microscopic degrees of freedom within "Sonderforschungsbereich 484" (cooperative phenomena in the solid state). During the winter term of 2001/2002, he stayed at the Kapitza Institute in Moscow within the scope of a Russian-German collaboration about defect states in low dimensional and magnetically frustrated systems. Currently, he is working on his habilitation thesis involving ESR in transition metal oxides.

Thomas Kurz is a PhD student in Augsburg (Germany). He obtained his Diploma in Physics about resistivity and magnetism in manganites in 2001. Since then, he has been working on his PhD thesis "magnetism in nanometer dimensions", which is a cooperation between the Philipps-University of Marburg (Germany) and the University of Augsburg. He is a member of the European Graduate College Marburg/Budapest. He stayed in Budapest (Hungary) as an exchange student in April 2003.

Prof. Dr. Alois Loidl is a full professor at the University of Augsburg. He studied Technical Physics in Vienna (Austria). In 1971, he finished his studies as a graduate engineer (Dipl.-Ing.) in nuclear physics and moved to the University of Frankfurt (Germany) where he performed his PhD in Solid State Physics. In 1981, he completed his Habilitation in Mainz (Germany) and was appointed professor (C2) at the Physical Institute in Mainz in 1983. After offers for a professorship from the University of Missouri-Columbia (Columbia, USA) and the University of Hannover (Germany), both in 1987, he was appointed as a university professor with tenure in Mainz. From 1991 to 1996, he was a full professor (C4) at the Institute of Solid State Physics at the Technical University of Darmstadt (Germany) and while there was also appointed executive director of the Physical Institute (1995). In 1996 he moved to the newly founded Center for Electronic Correlations and Magnetism at the University of Augsburg (Germany). He is an editor of the European Physical Journal B since 2000 and is author or coauthor of more than 400 scientific publications.

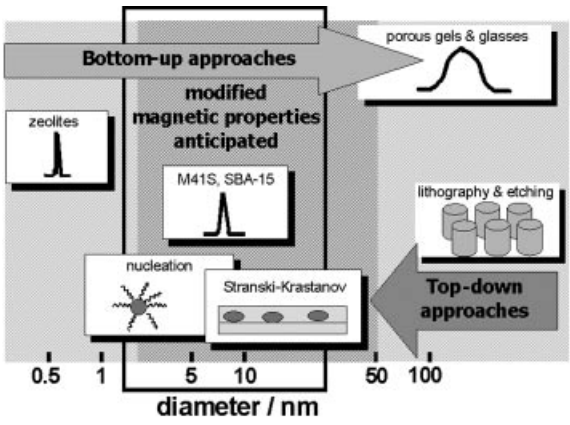

Figure 1. Bottom-up and top-down approaches for fabricating magnetic semiconductor nanostructures.

Alternatively, a large variety of so-called bottom-up approaches can be used to synthesise magnetic semiconductor nanostructures. Some of these approaches are also presented schematically in Figure 1. Examples are methods based on established growth techniques for 2D semiconductor structures (e.g. MBE or MOVPE) such as Stranski-Krastanov growth[10–18] or growth on patterned substrates.[19,20] There are also various fabrication techniques relying on nucleation and precipitation processes either in glass matrices (ranging from RF-sputtering techniques[21–24] to sol-gel methods[25–28]) or in solutions[29,30] (e.g. TOP/TOPO synthesis). All the bottom-up approaches mentioned so far yield good quality nanostructures down to sizes of a few nanometres. However, the ensembles of nanostructures fabricated in this fashion usually exhibit a rather broad Gaussian size distribution, which also manifests itself in measurements of the electronic and magnetic properties. In particular, in conventional magnetic measurements of such ensembles such as measurements of the magnetisation or of magnetic resonance, the results are strongly dominated by the larger magnetic particles, i.e. the "large size" wing of the distribution. The reason is very simple, such measurements are sensitive to the total number of magnetic ions and the amount of magnetic ions per nanostructure scales with its characteristic size e.g. for a spherical nanoparticle with the third power of its diameter. Therefore, it is desirable to define a sharp cut-off of the size distribution of the nanoparticles towards larger sizes.

One way of achieving this is by chemical synthesis of nanoparticle ensembles in a bottom-up approach using size-limiting matrices, which serve as a kind of "mini-reactor". Narrow particle size distributions can be obtained if a high quality of this nanoreactor is realised. As hosts for a size-limited synthesis only a few possibilities are worth considering: firstly, the utilisation of reverse micelles ("water-in-oil" droplets), which are already used widely in the synthesis of nanoparticles,[31–40] and secondly, the use of a porous substance which does not react with the precursors for the actual synthesis. In the large group of different porous substances the mesoporous materials seem to be the most promising approach for nanoparticle syntheses[41] since the size range, in which the pores – and therefore the nanoparticles – can be synthesised, covers a scale of several hundreds of nanometres and in particular sizes below 50 nm where changes of the particle properties due to confinement are anticipated (see also Figure 1).

In the case of reverse micelles the size of the micelle is governed by the volume of the water molecules inside and by the surfactant molecules at the surface of the micelle, i.e. the space inside the micelle where the chemical reaction or coprecipitation takes place can be varied for example by changing the amount of water in the original solution.[42] One of the surfactants often used to form reverse micelles in a nonpolar solvent is sodium di(2-ethylhexyl) sulfosuccinate, mostly denoted as Aerosol OT or Na(AOT). In a typical synthesis (see Figure 2), two micellar solutions, having the same water content (that is to say the same micelle size) and each containing one of the reactants, are mixed. When two of these micelles collide, they exchange their water contents in a micellar exchange process and the desired reaction occurs. After a few microseconds the previously formed "double-micelle" dissociates to form two independent reverse micelles, one containing the product while the other is only filled with water.

Figure 2. Micellar exchange process in a nonpolar solvent. The reaction takes place inside the water micelles (redrawn from ref.[42]).

When using mesoporous materials as hosts for the synthesis of nanoparticles, the narrow size distribution of the guest species is achieved by a narrow pore size distribution of the respective host material. In the last 12 years it has been a major goal in the synthesis of mesoporous substances to obtain materials which exhibit a high degree of long range order on the one hand and a narrow pore size distribution on the other. The quality of mesoporous materials has risen from poorly ordered so-called "disordered mesoporous foams" to high quality materials, which have very sharp pore size distributions. The high degree of long-range order can be demonstrated by TEM investigations or high-quality XRD measurements. A perfect arrangement of the pores over length scales of 300 nm and more is state of the art.[43]

Fine tuning of the pore size can be achieved by varying the nature of the structure directing agent (SDA). At first, long-chain tetraalkylammonium halides were used as SDA's for the synthesis of mesoporous materials of the M41S family. By varying the chain length of the hydrophobic alkyl group (usually containing 12 to 22 carbon atoms) the pore size can be altered very precisely in the range of about 1 nm.[44,45] However, the overall pore size is limited to about 4 nm when using these kinds of surfactants. The utilisation of swelling agents offered the possibility of expanding the

pore sizes to about 10 nm, but this was always accompanied with an overall loss of structural order, which was achieved in the first instance.

In 1998, new precursors for the synthesis of a new class of mesoporous materials were first introduced. These so-called triblock copolymers offer the possibility of expanding the pore size to about 30 nm.[46] Just by varying the synthesis temperature a fine tuning of the pore diameters was achieved and narrow size distributions with mean diameters in the range of 5 to 10 nm were obtained. However, the distributions do broaden when going to higher mean diameters.

Synthesising mesoporous materials with well defined pore diameters, i.e. narrow pore size distributions, is the first step to preparing reasonable hosts for the synthesis of nanoparticles which are formed inside the pores.

Introducing the precursor compounds into the pores of the respective size-limiting matrices is the next synthetic problem, which has to be addressed. The utilisation of reverse micelles has the advantage of a two-phase system. Using a precursor, which is only soluble in one of the phases (in this case water) prevents desired materials from forming outside of the mini-reactor and results in a very defined synthesis exclusively inside the size-limiting matrix.

In the case of mesopores as the size-limiting matrix, however, the formation of bulk materials outside the pore system can never be fully avoided. Only after the synthesis can one estimate the amount of bulk material formed during the synthesis. Wet impregnation techniques[41] and incorporation of the precursors from supercritical CO_2[47] can be applied to introduce guest molecules into the pores of the host material. Drying the impregnated materials is the crucial step in the synthesis to preventing the formation of bulk material on the outer surface of the host structure. After the introduction of the precursor the other reactants have to be introduced via the gas phase, which is to prevent the extraction of the first precursor from the pores and the consecutive precipitation outside the pores if the second reactant is introduced in a liquid form. Figure 3 gives a schematic representation of a mesopore directed synthesis of nanoparticles.

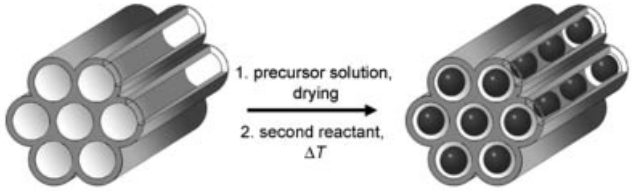

Figure 3. Schematic representation of nanoparticle synthesis inside a mesoporous host.

One of the most investigated semiconductor nanoparticles is cadmium sulphide, CdS.[2,10,31] The occurring quantum confinement, which is mostly reflected by a blue-shift of the band-gap energy, has been discussed extensively.[30,48–54] Other nanoscale semiconductor compounds, such as III-V semiconductors (e.g. GaAs or InP) or other II-VI semiconductors (e.g. CdSe, CdTe, ZnS, ZnSe, ZnTe), have also been studied in great detail (see recent reviews[42,55–58]), but to discuss all of them here would go beyond the scope of this micro-review. Instead, this work focuses on the synthesis and characterisation of Mn doped II-VI semiconductor nanostructures and describes in detail the effects of miniaturisation on the electronic, magnetic and optical properties of these materials.

The synthesis of the so-called "diluted magnetic semiconductor" (DMS) nanostructures is of great interest as semiconducting and magnetic properties are combined in one for the same nanostructure. Therefore, ordered arrays of nanometre-sized magnetic semiconductors are promising components for new devices in magneto- or spin electronics (e.g. magnetic hard disc media, non-volatile computer memory chips).[59] These materials are obtained, when a cation A of a binary semiconductor AB is randomly substituted by a magnetic ion M, leading to a $A_{1-x}M_xB$ formula. Physical properties, for example, band-gap energy or magnetic behaviour, are now not only a function of the particle size but also of the doping level x.

2. Synthesis

The first preparation of manganese doped ZnS nanoparticles with particle sizes ranging between 3.5 and 7.5 nm was reported by Bhargava et al. in 1994.[60] The quantum dots were synthesised by a precipitation approach in which diethylzinc and diethylmanganese in a toluene solution were treated with H_2S. However, in the case of liquid solution precipitation or self-organised growth methods, the particle size distribution is not very well defined. Similar results were also found in other approaches.[61–64] In particular, there is no sharp upper limit for the size, in contrast to the case of nanostructures synthesised inside nanoreactors such as reverse micelles or mesoporous materials. The existence of a sharp upper limit is desired in most investigations of the effects of reduced dimensions on the magnetic properties as the largest particles usually determine the results.

A synthesis of $Cd_{1-x}Mn_xS$ nanoparticles with a very sharp size distribution was reported by Pileni's group, by applying the reverse micelle technique.[65,66] The obtained particle sizes could be varied from an average size of about 1.8 to 3.2 nm and the reported manganese contents were $0 \leq x \leq 0.23$.

DMS nanoparticles were also synthesised inside mesoporous host structures. This approach for a host/guest system was first described in 2002 by our group, when $Cd_{1-x}Mn_xS$ was incorporated inside 3 nm wide pores of MCM-41 silica.[67] First, calcined MCM-41 silica was impregnated with an aqueous solution of cadmium and manganese acetate in the desired molar ratio. Afterwards the precipitate was filtered off, thoroughly dried and treated with H_2S at $T \leq 100$ °C. Powder X-ray diffraction and nitrogen physisorption proved the preservation of the host structure after the intrapore formation of the guest species and showed that the reaction had only taken place inside the pores and

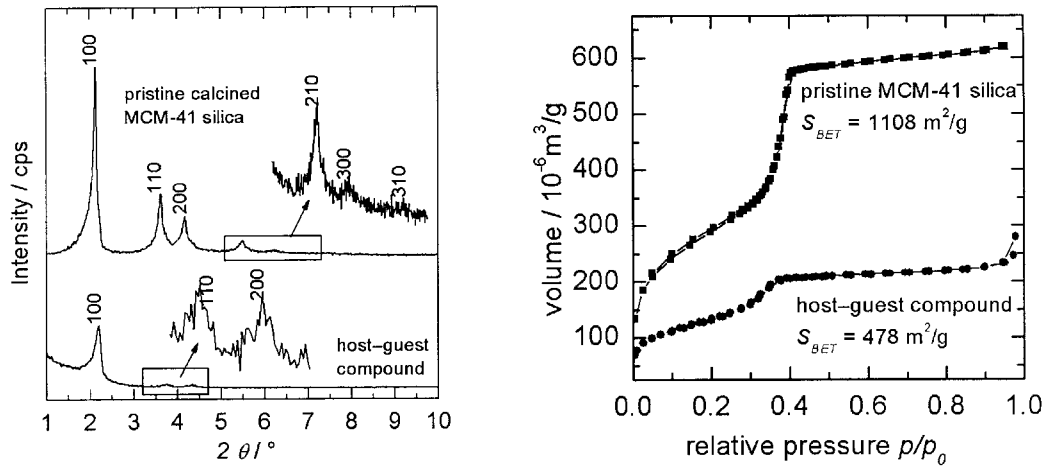

Figure 4. Powder X-ray diffraction patterns (left) and nitrogen physisorption isotherms (right) of MCM-41 silica and MCM-41 silica/$Cd_{1-x}Mn_xS$ host/guest compounds.[67]

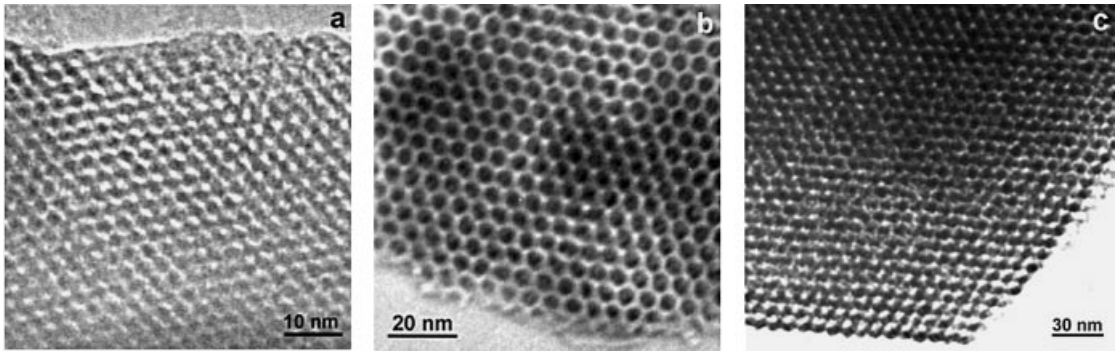

Figure 5. TEM pictures of different mesoporous host structures, a) MCM-41 silica with 3 nm pores, b) SBA-15 silica with 6 nm pores, c) SBA-15 silica with 9 nm pores.[70]

no bulk material was formed (Figure 4). The complete transformation of the acetates to the sulphides was proved by infrared and X-ray absorption spectroscopy. Similar results were obtained for other host/guest system based syntheses of nanoparticles, like $Cd_{1-x}Mn_xSe$ within MCM-41 silica[68] and $Cd_{1-x}Mn_xS$ within mesoporous thin films.[69]

A more detailed discussion on the size dependence of electronic, magnetic and optical properties was given in 2004, when the DMS compound $Zn_{1-x}Mn_xS$ was synthesised inside mesoporous hosts with different pore sizes.[70] For an accurate study three different mesoporous materials, each with cylindrical pores, were used: MCM-41 silica with 3 nm pores and furthermore two SBA-15 silica with 6 and 9 nm pores. The different pore sizes of the host materials were realised using different SDA's and different reaction temperatures (see above). A very high degree of order of the host materials was achieved, which was apparent from X-ray diffraction, sorption analyses and TEM investigations (see Figure 5).

The intrapore formation of the nanoparticles was carried out the same way as described for the $Cd_{1-x}Mn_xY$ (Y = S, Se) nanoparticle preparation, only this time the impregnation/conversion cycle was repeated several times to achieve a higher filling of the pores. Again, no bulk material was formed outside the respective pore system and the mesostructure was still found to be intact after the synthesis.

3. Band Gap and Optical Properties

With photoluminescence-spectroscopic techniques it is possible to measure the dependence of the band-gap variation on particle size and doping level x. This was carried out for various DMS compounds, like $Cd_{1-x}Mn_xS$,[66–68,71,72] $Cd_{1-x}Mn_xSe$[68] and $Zn_{1-x}Mn_xS$,[70,73] synthesised either in reverse micelles or in mesoporous hosts.

Figure 6 shows a schematic diagram of the complex optical processes observable in wide-gap (II,Mn)VI semiconductors. The semiconductor band states with a direct band-gap transition and the 3d shells of the Mn^{2+} ions with their internal transitions form electronic subsystems of the (II,Mn)VI semiconductor which are coupled by energy transfer processes. In addition to semiconductor band-gap related luminescence and absorption, luminescence and absorption bands are observed due to the intra-3d-shell transitions of the Mn^{2+} ions. The states within the 3d shell are strongly affected by the crystal field of the lattice site of the corresponding Mn^{2+} ion. The majority of the Mn^{2+} ions

are incorporated on cation sites with a tetrahedral crystal field. The lowest state is the $^6A_1$ state originating from the ^6S state of the free ion, and the next highest states are $^4T_1$, $^4T_2$, $^4A_1$ and ^4E originating from the ^4G state of the free ion. Absorption processes can take place between the $^6A_1$ ground state and the excited states. A yellow luminescence between the $^4T_1$ first excited state and the $^6A_1$ ground state is observed for all wide-gap (II,Mn)VI compounds, independent of Mn concentration for Mn incorporated onto the cation site. In addition, there are a few Mn^{2+} ions on other sites. These "defect" sites show a different crystal field splitting between the states of the 3d shell, and this leads to other absorption and luminescence bands. A prominent example is the red Mn^{2+} luminescence. Energy-transfer processes can take place between the band states and the Mn^{2+} 3d shells, as well as between Mn^{2+} 3d shells corresponding to different sites.

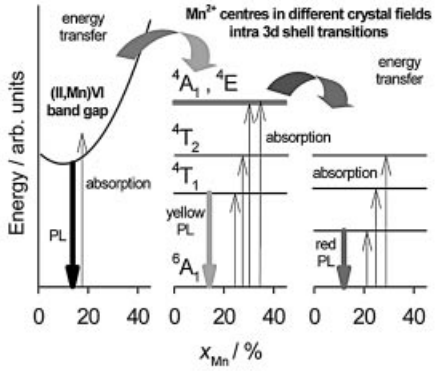

Figure 6. Schematic diagram of the optical processes observable in wide-gap (II,Mn)VI semiconductors. The abscissa values are the same for all three graphs.

In Figure 7 typical optical spectra of $Zn_{0.7}Mn_{0.3}S$ nanoparticles synthesised inside mesoporous hosts with different pore diameters are shown. The PL spectrum is dominated by the strong yellow luminescence originating from the $^4T_1 \rightarrow {}^6A_1$ internal Mn^{2+} 3d shell transition (exemplarily shown for the 6 nm sample, thick line in Figure 7).

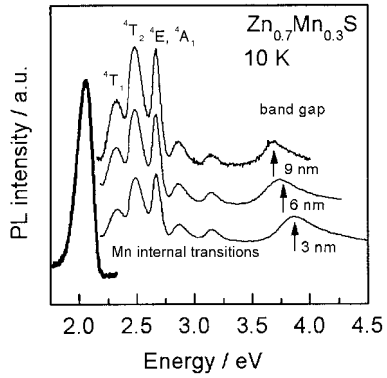

Figure 7. PLE spectra (thin lines) of $Zn_{1-x}Mn_xS$ nanoparticles with diameters of 3, 6 and 9 nm, respectively, detected on the yellow Mn luminescence. The Mn-related yellow PL band (thick line) of the 6 nm sample is shown as a typical example.

The internal Mn transitions arising from the $^4T_1$, $^4T_2$, ^4E and $^4A_1$ states are observable between 2.3 and 2.7 eV (the increase in intensity with increasing particle size simply reflects the increasing total amount of manganese) whereas the peak at the highest energy in each spectrum corresponds to the band gap related absorption. Because of the effective energy transfer from the band states into the Mn subsystem this peak is also detectable on the yellow PL.

The band gap related feature shifts to higher energies with decreasing particle diameter (i.e. shows a quantum confinement effect) whereas the energy positions of the Mn^{2+} internal transitions remain unaffected by the particle size (demonstrating that the energy positions are only determined by the local crystal field of the Mn site). The observed quantum confinement effects prove that during the synthesis $Zn_{1-x}Mn_xS$ is formed inside the SiO_2 pore system only. The energy positions of the Mn^{2+} internal transitions serve as a probe of the crystal field at the Mn site. In Figure 8 the energies of the lowest excited states of a Mn^{2+} $3d^5$ ion in a T_d symmetric ligand field with respect to the $^6A_1$ ground state are depicted for a bulk $Zn_{0.9}Mn_{0.1}S$ sample (full circles) and the $Zn_{0.7}Mn_{0.3}S$ nanostructures of different radii (open symbols). The curves have been calculated in the Tanabe–Sugano model[74] as a function of the crystal field parameter Dq with the Racah parameters B = 50 meV and C = 434 meV. The extracted crystal field parameters using the Tanabe–Sugano method are almost the same for bulk samples and nanostructures indicating the good quality of the nanostructures.

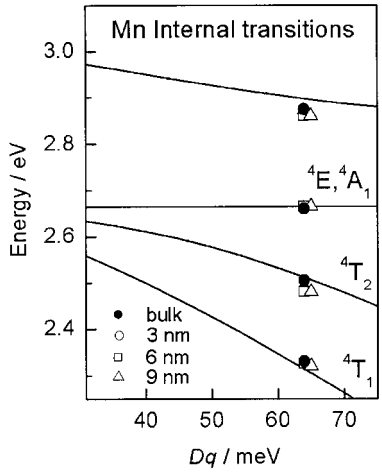

Figure 8. Energies of the internal transitions of Mn^{2+} ions in a T_d symmetric crystal field versus the field parameter Dq using the Racah parameters B = 50 meV and C = 434 meV, calculated in the framework of the Tanabe–Sugano model. Experimental points for $Zn_{0.9}Mn_{0.1}S$ bulk and $Zn_{0.7}Mn_{0.3}S$ nanostructures.

Figure 9 gives a comparison of the energy positions of the band gaps of nanoparticles of three (II,Mn)VI DMS's with different diameters as a function of Mn content x. A bulk reference curve is shown in the case of $Cd_{1-x}Mn_xSe$, but not for $Zn_{1-x}Mn_xS$ and $Cd_{1-x}Mn_xS$. For the sulphides, the band gaps of the 9 nm nanostructures are almost bulk-like. The quantum confinement of the excitons in the nano-

particles evokes an increase in the direct band gap of about 350 meV for 3 nm $Cd_{1-x}Mn_xSe$ nanoparticles compared with the bulk. For the corresponding $Cd_{1-x}Mn_xS$ nanoparticles the confinement is only about 200 meV. In the case of the 3 nm $Zn_{1-x}Mn_xS$ nanoparticle the confinement energy compared to the bulk is about 180 meV. The decrease of the confinement energy going from (Cd,Mn)Se via (Cd,Mn)S to (Zn,Mn)S has two major reasons: (1) the exciton Bohr radius decreases throughout the series and (2) the corresponding bulk band gap increases, i.e. reduces the height of the confining potential given by the band-gap difference between the SiO_2 barrier and (II,Mn)VI semiconductor. The (Cd,Mn)S as well as the (Zn,Mn)S nanoparticle series clearly show, as expected, that the confinement effects increase with decreasing particle diameter. For both series the energy positions for the 9 nm wires almost correspond with those of the bulk band gaps.

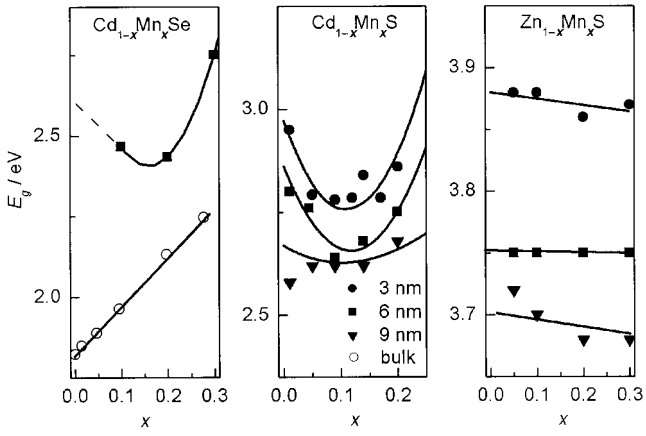

Figure 9. Band gaps of $Cd_{1-x}Mn_xSe$ nanoparticles (left), $Cd_{1-x}Mn_xS$ nanoparticles (middle) and $Zn_{1-x}Mn_xS$ nanoparticles (right) of different diameters as a function of composition x at $T = 10$ K. The solid lines are guides to the eye.

An interesting result is that both Cd-based nanoparticle systems exhibit a larger bowing of the band gap, depending on the Mn concentration, than do the corresponding bulk samples. This agrees with results reported for (Cd,Mn)S quantum dots by Levy et al.,[66] who also showed that the exchange interaction-induced band gap bowing becomes stronger with decreasing diameter for (Cd,Mn)S quantum dots synthesised in reverse micelles. Such a bowing is known for various bulk wide-gap (II,Mn)VI semiconductors.[75–78] Bylsma et al. derived the following expression for the band gap as a function of temperature T and Mn concentration x in DMS nanostructures [Equation (1)]:[79]

$$E_g(x,T) = E_0 + \Delta E x - \frac{AT^2}{T+B} - C\chi T \quad (1)$$

where the first three terms represent the commonly used description of the energy gap of a semiconductor compound comprising a linear shift in composition and a Varshni-like temperature dependence. The last term is specific to DMS and causes the bowing. It describes a contribution due to the magnetic susceptibility χ of the Mn ions. Both, the constant C as well as magnetic susceptibility χ, may be affected by the reduction of the lateral dimensions. The constant C is given by Equation (2).

$$C \sim 3m_c\alpha^2 + (m_{hh} + m_{lh})\beta^2 \quad (2)$$

where m_c, m_{hh}, and m_{lh} are the conduction-band and valence-band masses and α and β are the s–d and p–d coupling parameters. As $\alpha << \beta$ and m_{hh}, $m_{lh} > m_c$ in the (II,Mn)VI compound, the magnitude of C is mainly determined by β for which Larson et al. give the following expression [Equation (3)]:[80]

$$\beta = -32\frac{V_{pd}^2}{N_0}\left[\frac{U_{eff}}{(E_d + U_{eff} - E_{ev})(E_v - E_d)}\right] \quad (3)$$

where V_{pd} and U_{eff} are a hopping parameter depending on the manganese–anion distance and an electron-electron interaction parameter in the Hubbard fashion. The hopping parameter V_{pd} basically represents the hybridisation between the Mn 3d orbitals and the anion p orbitals in the bonding of the ternary (II,Mn)VI semiconductor compound. In the band structure of the (II,Mn)VI compound this is reflected by the energetic overlap of the anion p-orbital derived valence bands and the Mn 3d-orbital derived valence bands in the density of states as shown schematically on the left hand side of Figure 10. The electron-electron interaction parameter U_{eff} represents the on-site Coulomb repulsion energy which is required to add a sixth electron to the half-filled Mn 3d shell as shown schematically on the right of Figure 10. E_v and E_{3d} are representative energies of the p-like valence-band edge states and the Mn 3d related valence-band states, respectively.

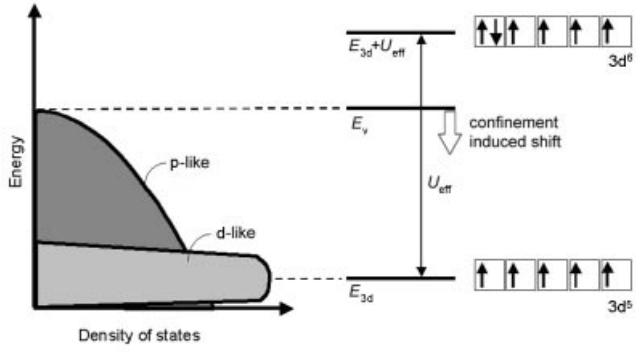

Figure 10. Schematic representation of the parameters contributing to the p–d exchange parameter β in the model by Larson et al.

The p–d coupling parameter β strongly depends on the energy separation between the p- and d-like valence-band states represented by E_v and E_{3d}, respectively [see Equation (3)]. The modified positions (compared to bulk) of the p- and d-related bands in the band structure of the nanoparticle causes an increase of the p–d exchange interaction, resulting in a possible contribution to the enhanced band-gap bowing in the nanostructures. Due to the quantum confinement, the top of the p-like valence band (E_v) of the $Cd_{1-x}Mn_xS$ nanostructures may shift significantly towards the Mn 3d states (E_{3d}), which are positioned about 3 eV below

the valence-band edge of bulk material (see Figure 10). This enhancement effect is similar to that in bulk $Cd_{1-x}Mn_xY$ with Y = Te, Se, S where an increased p–d hybridization is observed with increasing band gap going from Te to S.[81] Similar results were also reported for the corresponding Zn series where the main Mn 3d photoemission feature was found at 3.5, 3.6 and 3.8 eV below the valence-band maximum of (Zn,Mn)Te, (Zn,Mn)Se and (Zn,Mn)S, respectively.[82]

The susceptibility χ itself is also affected by the reduced dimensionality. In virtual crystal and mean-field approximation, the expression for χ is given by Equation (4):

$$\chi = x_{\text{eff}} \frac{N_A S(S+1) g^2 \mu_B{}^2}{3k_B[T + \Theta(x)]} \quad (4)$$

x_{eff} (which is a magnetically effective Mn concentration accounting for antiferromagnetic pairing) as well as $\Theta(x)$ are modified in a nanostructure due to the increase of the surface-to-volume ratio. The number of nearest neighbours on the cation sublattice is reduced at the surface leading to an increase of the effective x. This also causes a reduction of the Curie–Weiss parameter Θ in a similar fashion (see section 4: "Magnetic properties"). The combination of both effects results in a stronger increase of χ with x in the nanostructures compared to the bulk.

Therefore, both the dependence of the p–d exchange parameter β and that of the susceptibility χ on reduced dimensionality are in accordance with the observed enhancement of the band-gap bowing in $Cd_{1-x}Mn_xS$ and $Cd_{1-x}Mn_xSe$ nanostructures as a function of x. It is worth mentioning here that the former effect is probably of less importance because a good description of the magnetic properties of the paramagnetic phase of the (II,Mn)VI nanostructures is obtained (see section 4), assuming that the exchange coupling between adjacent Mn ions J_{nn} (which is proportional to β^2) is not altered in the nanostructures. Moreover, the dependence of the band gap of bulk $Zn_{1-x}Mn_xS$ and the corresponding nanostructured samples on the Mn concentration x seems to be an exception from a general rule. Although bulk (Zn,Mn)Te[75,83] as well as (Zn,Mn)Se[76,79] exhibit considerable bowing effects, neither the bulk $Zn_{1-x}Mn_xS$[84] nor the nanostructured samples in Figure 9 exhibit significant bowing effects with increasing x.

4. Magnetic Properties

Undoped II-VI compounds (x = 0) are diamagnetic whereas Mn–VI compounds (x = 1) are paramagnetic at high temperatures and exhibit an antiferromagnetic phase at low temperatures. The degree of magnetic coupling between the spins of the Mn ions depends strongly on the average distance between them, i.e. on x. Consequently, a very rich magnetic phase diagram as a function of x and T arises for a typical (II,Mn)VI semiconductor alloy such as (Cd,Mn)S (see Figure 11). Decreasing the concentration x of magnetic ions in diluted magnetic II-VI alloys restricts the spin ordering effects to the lower temperature region. Nevertheless, phases determined by collective magnetic behaviour such as antiferromagnetic (AF) phases as well as a spin-glass phase (SG) are commonly observed in addition to the paramagnetic phase (P) (Figure 12 gives a schematic summary of collective and individual behaviour of magnetic systems). The P phase extends to lower temperatures with decreasing x. For example, for (Cd,Mn)S, a (disordered) AF phase which has a long-range spin ordering occurs below a critical temperature $T_N(x)$ for a sufficiently high Mn concentration $x > 0.8$ (beyond the miscibility gap). The corresponding phase transition is characterised by peaks at T_N in both the magnetic susceptibility and the specific heat. For Mn concentrations below the miscibility gap an SG phase is observed for temperatures below $T_{SG}(x)$. In the case of (Cd,Mn)Te even a transition to the AF phase has been reported for x = 0.7,[85] which means that it is still below the miscibility gap.

The spin-glass phase is characterised by an antiferromagnetic short-range ordering of the spins, as well as by frustration effects. The somewhat diffuse phase transition from the paramagnetic into the spin-glass phase leads to a peak at $T_{SG}(x)$ in the temperature dependence of the magnetic susceptibility, but no anomaly in the specific heat is observable. Neutron-scattering experiments have shown that small antiferromagnetically ordered clusters already appear above T_{SG}, which grow in size with decreasing temperature. Another surprising fact is that a spin-glass phase is observable not only above the percolation limit ($x \approx 0.2$), but also below. In the very low concentration range, a rather long-range interaction is necessary, in addition to the short-range superexchange interaction, to yield a spin-glass phase. The

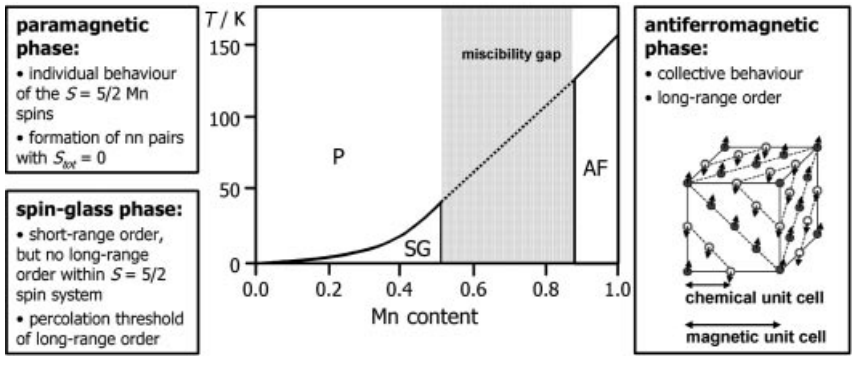

Figure 11. Schematic representation of a typical magnetic phase diagram of a (II,Mn)VI semiconductor.

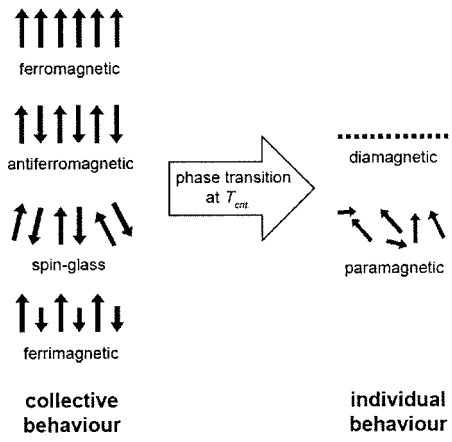

Figure 12. Schematic representation of the collective to the individual behaviour of magnetic systems.

spin freezing temperatures below the percolation concentration are very small, for example, between 0.1 K and 1 K for $x \approx 0.01$. The magnetic dipole-dipole interaction between more distant Mn^{2+} ions is proposed to be the required long-range interaction responsible for this spin-ordering mechanism, despite the fact that the dipole-dipole interaction might be too weak to cause the ordering at finite temperatures.[86]

In bulk (II,Mn)VI materials, the integral EPR signal corresponding to the Mn^{2+} absorption has a Lorentzian lineshape in the paramagnetic regime.[87] The overall intensity I_{tot} as well as linewidth ΔH of the Lorentzian are very sensitive to the spin-spin correlations between the Mn^{2+} ions. Not only changes of the magnetic order with temperature, e.g. transitions from the P phase to the SG phase or from the P phase to the AF phase, are reflected by the temperature dependence of ΔH and I_{tot}, but also by changes of the magnetic interactions within the paramagnetic phase itself due to a reduction of the lateral dimensions.

The EPR spectra for (II,Mn)VI nanoparticles synthesised either in reverse micelles or inside mesoporous hosts are very similar. As a typical example, the EPR spectra of $Zn_{1-x}Mn_xS$ nanoparticles with x varying from 0.01 to 0.3 synthesised inside the 6 nm wide pores of SBA-15 silica are shown in Figure 13.[70] All spectra were taken at 4 K and normalised to the same amplitude. These spectra are typical for exchange coupled Mn^{2+} ions within a II-VI semiconductor compound[88–90] and in nanostructured DMS compounds, for example $Cd_{1-x}Mn_xS$[91] and $Zn_{1-x}Mn_xS$.[70] The spectra can best be explained for low x. They basically consist of a sextet of sharp lines. This sextet, which is centred at a g value of $g = 1.999$, is associated with the allowed ($\Delta m_S = \pm 1$, $\Delta m_I = 0$) magnetic dipolar transitions between the hyperfine-split Zeeman levels of the $^6S_{5/2}$ (or, $^6A_1$) ground state of the Mn^{2+} 3d electrons. The hyperfine structure arises from the interaction between the $S = 5/2$ spin of the unpaired 3d electrons with the $I = 5/2$ spin of the ^{55}Mn nucleus. The hyperfine splitting characteristic for Mn^{2+} in ZnS amounts to about $\delta B_{HFS} = 7.0$ mT between neighbouring allowed transitions in zinc blende as well as in wurtzite structures.[10] The splitting observed in the spectrum of the sample with 1% Mn agrees well with this value.

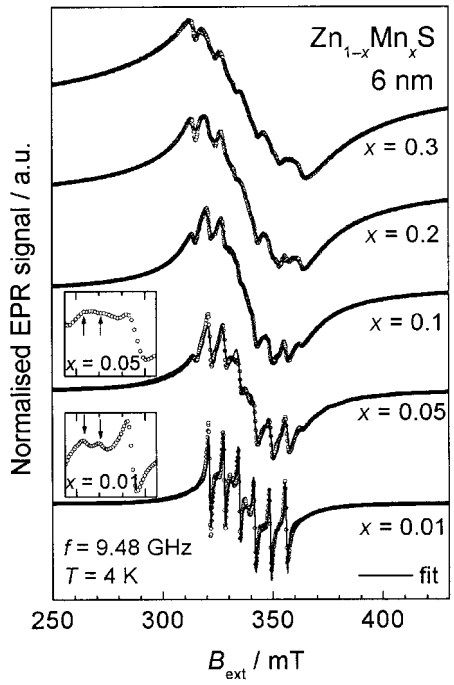

Figure 13. EPR spectra of 6 nm $Zn_{1-x}Mn_xS$ nanoparticles with x varying from 0.01 to 0.3 at $T = 4$ K. Insets: hyperfine transitions on an enlarged field scale for $x = 0.01$ (lower) and $x = 0.05$ (upper), the arrows indicate the positions of the forbidden transitions. Taken from ref.[70].

With increasing Mn content the dipolar interaction and exchange coupling merge the hyperfine structure into one broad resonance line, which is documented best for $x = 0.3$. But this broad line can already be identified for $x = 0.01$. The spectrum for $x = 0.01$ is satisfactorily described by the sum of the broad line and the hyperfine structure of six lines. Both the broad line and the hyperfine lines were assumed to be of Lorentzian shape. In addition it was necessary to take into account a slight linear increase of the hyperfine splitting with the external field due to second-order contributions.

A close inspection reveals that at low Mn concentration each hyperfine line exhibits a pair of satellites at lower external magnetic field associated with the forbidden ($\Delta m_S = \pm 1$, $\Delta m_I = \pm 1$) hyperfine transitions (see lower inset of Figure 13). The forbidden hyperfine transitions in the spectra with the lowest manganese content ($x = 0.01$) are typical for Mn^{2+} ions in the tetrahedral environment of a Zn site in a zinc blende crystal. In the case of a wurtzite crystal these lines are much more prominent and merge with the lines of the allowed hyperfine transitions, as is observed for samples with larger amounts of manganese ($x \geq 0.05$, see upper inset of Figure 13). Thus, it can be concluded that the crystal structure of the incorporated (II,Mn)VI semiconductors is zinc blende only for $x = 0.01$, whereas higher doping levels with Mn^{2+} result in a wurtzite structure. At the same time it has to be noticed that with increasing x an additional hyperfine structure of six lines with a

larger splitting of about δB_{HFS} = 9.5 mT evolves and persists even at 30% Mn content. This hyperfine structure results from isolated Mn^{2+} ions on the surface of the $Zn_{1-x}Mn_xS$ nanoparticles. From a careful analysis of the intensities of the different signals it can be deduced that the majority of the Mn^{2+} ions are well incorporated into the $Zn_{1-x}Mn_xS$ nanostructures and only a small amount remains weakly bound at their surface.[92] This amount of aggregated Mn ions at the surface of the nanoclusters corresponds to less than 4% of the total amount of Mn in the nanostructure.[70]

The Curie–Weiss parameter Θ of the paramagnetic phase is a measure of the type and strength of the interaction between the manganese ions. It can be obtained experimentally either from plots of the inverse EPR intensity I_{tot}^{-1} versus temperature T or from plots of the inverse susceptibility χ^{-1} versus temperature determined by SQUID measurements. It is found that the experimentally determined Cure–Weiss parameter is usually well described in the high-temperature limit using Equation (5):[93,94]

$$\Theta(x) = -\frac{2}{3k_B}S(S+1)x[J_{nn}z^b_{nn} + J_{nnn}z^b_{nnn}] \quad (5)$$

where J_{nn} and J_{nnn} are the nearest neighbour (nn) and next-nearest neighbour (nnn) exchange coupling constants, respectively, between Mn ions on the cation lattice. The numbers of nn and nnn sites of the cation lattice are denoted by z_{nn} and z_{nnn}, respectively. For both wurtzite and zinc blende crystals z^b_{nn} and z^b_{nnn} are 12 and 6 respectively, in the bulk.

Figure 14 shows plots of the inverse EPR intensity I_{tot}^{-1} of 9 nm $Zn_{1-x}Mn_xS$ nanoparticles with x ranging from 0.01 to 0.3 as a function of the temperature. Similar results were also obtained for a series of $Cd_{1-x}Mn_xS$ nanoparticles with 3 to 9 nm diameters and a series of $Zn_{1-x}Mn_xS$ particles with diameters of 3 and 6 nm, each synthesised within mesoporous hosts. As in the case of bulk (II,Mn)VI, the slope of the $I_{tot}^{-1}(T)$ curve decreases with increasing doping level x and deviates from the Curie–Weiss behaviour at low temperatures, giving the curves a somewhat negative curvature. At first sight surprisingly, the particles with $x \geq 0.2$ do not show any indication for a phase transition into a spin-glass phase, in contrast to bulk material.[95] This result will be discussed further, when the EPR linewidth is analysed. Fitting the $I_{tot}^{-1}(T)$ plots in the high temperature regime (200 K to 300 K) following the Curie–Weiss dependence [Equation (6)]:

$$I_{tot}^{-1}(T) \sim \chi^{-1}(T) \sim (T + \Theta) \quad (6)$$

yields the Curie–Weiss parameter Θ as a function of x.

The corresponding plots for various particle diameters d (obtained by analysing the corresponding EPR data, as shown exemplarily for x = 0.1 in Figure 14, where a straight line is used for extracting the high-temperature Curie–Weiss parameter Θ) are shown in Figure 15 and show some clear trends. As expected, $|\Theta|$ increases with increasing x in each series. The $|\Theta|$ values obtained for the nanostructures are considerably lower than those found in corresponding bulk

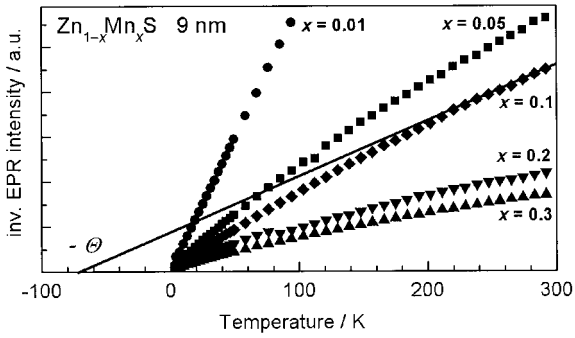

Figure 14. Temperature dependence of the inverse EPR intensity I_{tot}^{-1} of 9 nm $Zn_{1-x}Mn_xS$ nanoparticles.

(II,Mn)VI samples. These are represented by the solid lines in Figure 15 and are calculated using Equation (5). The exchange parameters are taken from the literature:[94,96] J_{nn} = –10.6 K and J_{nnn} = –4.7 K for (Cd,Mn)S and J_{nn} = –16.1 K and J_{nnn} = –0.6 K for (Zn,Mn)S. Moreover, in Figure 15, it appears that the $|\Theta|$ values show a tendency to decrease with decreasing particle diameter d at constant x. Both effects are due to the reduced lateral dimensions of the nanostructures. They occur because Mn ions on the surface of the (II,Mn)VI nanostructures incorporated inside the mesoporous SiO_2 matrices have reduced numbers of nearest neighbours $z^s_{nn} \approx z^b_{nn}/2$ and next-nearest neighbours $z^s_{nnn} \approx z^b_{nnn}/2$ compared to the bulk of the material. This becomes significant as the surface-to-volume ratio is strongly increased in the nanostructures. The effect can be estimated by dividing the volume V of the nanostructure into a volume V^s close to the surface (where the exchange effects differ from bulk) and a remaining bulklike volume $V^b = V - V^s$. The choice of the two volumes will differ for nearest neighbours and next-nearest neighbours because of the length of the scales involved, i.e. the nearest neighbour distance d_{nn} and the next-nearest neighbour distance d_{nnn}, are different. In the following the wurtzite structure is approximated by a zinc blende structure for simplicity. This is a good approximation here as only nearest and next-nearest

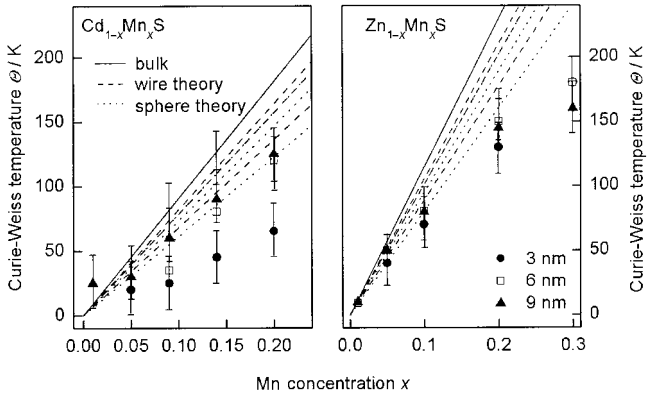

Figure 15. Plots of the Curie–Weiss temperature Θ versus Mn content x in percent obtained by analysing the EPR data of 3, 6, and 9 nm $Cd_{1-x}Mn_xS$ particles (left) and 3, 6, and 9 nm $Zn_{1-x}Mn_xS$ particles (right). The solid line is calculated using Equation (5), the dashed and dotted lines are calculated using Equation (8).

neighbours are considered. It holds that $d_{nn} = (1/2)^{0.5}a$ and $d_{nnn} = a$ where a is the lattice constant of the zinc blende lattice, $a \approx 0.55$ nm for (Zn,Mn)S and $a \approx 0.58$ nm for (Cd,Mn)S.[97] These values of the lattice constant were used for $Cd_{1-x}Mn_xS$ and $Zn_{1-x}Mn_xS$ independent of x in the following because its dependence on x is not known for the zinc blende modification. Two limiting cases for the shape of the nanostructure shall be considered: (i) an ideal wire structure of infinite length and diameter d and (ii) a spherical nanoparticle with diameter d where d is the pore diameter of the SiO_2 host matrix. One obtains the following definitions [Equation (7)]:

$$V^s_{nn} = V\left(1-\left(\frac{d-2d_{nn}}{d}\right)^{\delta}\right) \qquad V^s_{nnn} = V\left(1-\left(\frac{d-2d_{nnn}}{d}\right)^{\delta}\right) \tag{7}$$

with $\delta = 2$ for infinite wires and $\delta = 3$ for spheres. In both cases it holds that $V^b_{nn} = V - V^s_{nn}$ and $V^b_{nnn} = V - V^s_{nnn}$.

Rewriting Equation (5) including surface effects yields Equation (8).[91]

$$\Theta(x,d) = -\frac{2S(S+1)x}{3Vk_B}\left[J_{nn}\left(V^b_{nn}z^b_{nn}+V^s_{nn}z^s_{nn}\right)+J_{nnn}\left(V^b_{nnn}z^b_{nnn}+V^s_{nnn}z^s_{nnn}\right)\right] \tag{8}$$

Using Equations (5) and (8), the Curie–Weiss parameters have been calculated for $Cd_{1-x}Mn_xS$ and $Zn_{1-x}Mn_xS$ nanostructures assuming a wirelike and a spherical shape. Both the calculations, for the $Cd_{1-x}Mn_xS$ nanostructures as well as for the $Zn_{1-x}Mn_xS$ nanostructures, were carried out for d values of 3, 6, and 9 nm. The results of the calculations are also plotted in Figure 15. In both graphs, the dotted and dashed lines represent the results for a wirelike and a spherical shape, respectively. There are three calculated Θ curves for wire-shaped and three calculated Θ curves for sphere-shaped nanoparticles. For the wire and sphere shapes, the curves are assigned as follows to the corresponding d-values; the steepest curve corresponds to $d = 9$ nm, the intermediate curve to $d = 6$ nm and the least steep curve to $d = 3$ nm. Comparing experimental data and theoretical curves indicates that the theoretically derived reduction of the Curie–Weiss parameters Θ due to surface effects are, as expected, stronger for spherical nanoparticles compared to wire-shaped nanoparticles. The calculated reductions are of the right magnitude for both (Cd,Mn)S and (Zn,Mn)S nanostructures, but still smaller than those found in the experiment. Assuming that spherical particles yields a better agreement, this is in accordance with the TEM analysis of the (II,Mn)VI nanostructures. Figure 16 depicts a TEM image of (Zn,Mn)S nanostructures incorporated into an SBA-15 mesoporous SiO_2 matrix with a pore diameter d of 6 nm in a cross sectional view. The narrow "white" lines represent the SiO_2 walls of the pore systems. The dark regions are the (Zn,Mn)S nanoparticles. This view perpendicular to the pores reveals that the aligned pore channels are filled with the (Zn,Mn)S compound. It can clearly be seen that single "sphere-like" nanoparticles are present, but also that there is a tendency for these nanoparticles to agglomerate to denser "wire-like" structures. There is no evidence for larger particles being formed outside the pore system, i.e. the entire (Zn,Mn)S is confined inside the channels of the mesoporous host.

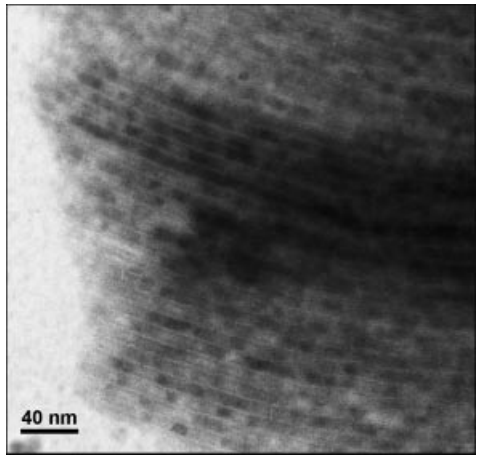

Figure 16. TEM image of (Zn,Mn)S nanostructures incorporated into 6 nm wide pores of SBA-15 silica.

In paramagnetic systems such as the (II,Mn)VI semiconductors, the EPR linewidth behaviour depends intimately on the physics of the inter-manganese spin-spin interactions. The EPR linewidth of bulk (Cd,Mn)- and (Zn,Mn)-chalcogenides has been widely studied.[87,98–101] The experimental results give a consistent picture, which can be summarized as follows: (i) In general, the EPR linewidth is found to increase with increasing Mn content and with decreasing temperature. The EPR line shape is Lorentzian for all samples in the paramagnetic regime. (ii) The EPR linewidth depends very strongly on the anion, i.e. Te, Se and S. For comparable Mn contents x and temperature T, it is found that the EPR line becomes broader as the atomic number of the anion increases from S to Se to Te.[87,98] (iii) There is a much weaker dependence on the type of nonmagnetic cation. The EPR line broadens as the atomic number of the cation decreases, e.g. $Zn_{1-x}Mn_xS$ signals are somewhat weaker and broader than $Cd_{1-x}Mn_xS$ signals for the same x and T.[98]

The EPR linewidth in manganese doped II/VI semiconductors with a high doping level x is found to diverge at low T due to the magnetic phase transition from the paramagnetic phase to the spin-glass phase, in particular for $x > 0.2$, i.e. above the percolation threshold in three dimensions. This additional broadening of the EPR linewidth occurs due to the divergence of the spin-spin correlation length in the vicinity of the paramagnetic to spin-glass phase transition. It is accompanied by a change of the EPR line shape, which becomes asymmetric.

As mentioned earlier $Zn_{1-x}Mn_xS$ and $Cd_{1-x}Mn_xS$ nanoparticles with $x \leq 0.3$ synthesised in mesoporous hosts do not show any signs of a paramagnetic to spin-glass phase transition. This is further substantiated by the correspond-

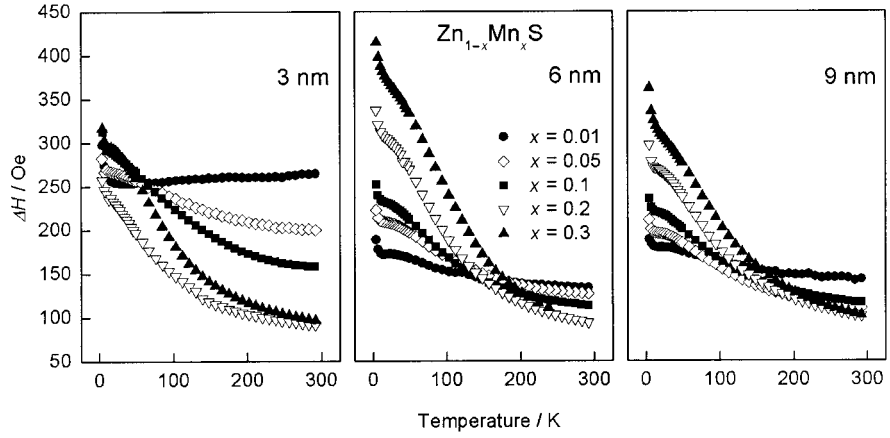

Figure 17. Plots of the EPR linewidth ΔH versus temperature for $Zn_{1-x}Mn_xS$ nanoparticles of different doping levels x and diameters of 3 nm (left), 6 nm (middle) and 9 nm (right).

ing EPR linewidths data in Figure 17 where the linewidth remains finite even at the lowest temperature. The critical Mn concentration x, above which the phase transition occurs, corresponds to the percolation threshold for the Mn ions on the cation sublattice. Obviously, the percolation threshold is increased due to the reduction of the lateral dimensions of the nanostructures and, thus, the magnetic phase transition is suppressed in the nanoparticles. Therefore, the linewidth behaviour is solely determined by the spin-spin interactions within the paramagnetic Mn subsystem.

In the following, the concentration dependence of the linewidth at low temperatures (T = 30 K) and at high temperatures (T = 290 K) will be analysed in more detail. Figure 18a and Figure 18b show plots of the linewidth at these temperatures for $Zn_{1-x}Mn_xS$ nanoparticles with different diameters and $Cd_{1-x}Mn_xS$ nanoparticles with different diameters, respectively. For both material systems, it can be seen from the left graphs that, at T = 30 K, the linewidth depends almost linearly on x. This can be understood as follows. At these temperatures the broadening is determined by a dipolar contribution in addition to an almost constant hyperfine contribution H_{HF}. Exchange narrowing effects due to nearest-neighbour exchange J_{nn} are negligible as basically all Mn ions with manganese nearest neighbours have formed antiferromagnetic pairs. The linewidth at low temperature can be described by Equation (9):

$$\Delta H = H_{HF} + H_{dip} \approx H_{HF} + C_{dip}x \quad (9)$$

where H_{dip} is the dipolar field at the site of a Mn ion in mean-field approximation.[102] The fits in the left graphs of Figure 18 show that the low temperature approximation in Equation (9) describes the observed linewidth behaviour in the nanoparticles very well, in particular for the 6 nm and 9 nm samples of both series. For the (Zn,Mn)S system, the value of H_{HF} of about 150 Oe determined for the 6 nm and 9 nm samples corresponds to half the extension of the six fine structure satellites in Figure 13. The value for the 3 nm samples is slightly larger. The linewidths of the series of $Cd_{1-x}Mn_xS$ nanoparticles show a similar dependence as that of the corresponding Zn-based series, but the linewidth is always smaller. It is worth pointing out that, as in bulk material, this simply reflects the difference in the cation size.

The high temperature behaviour [right graphs of Figure 18a and Figure 18b] can be explained semiquantita-

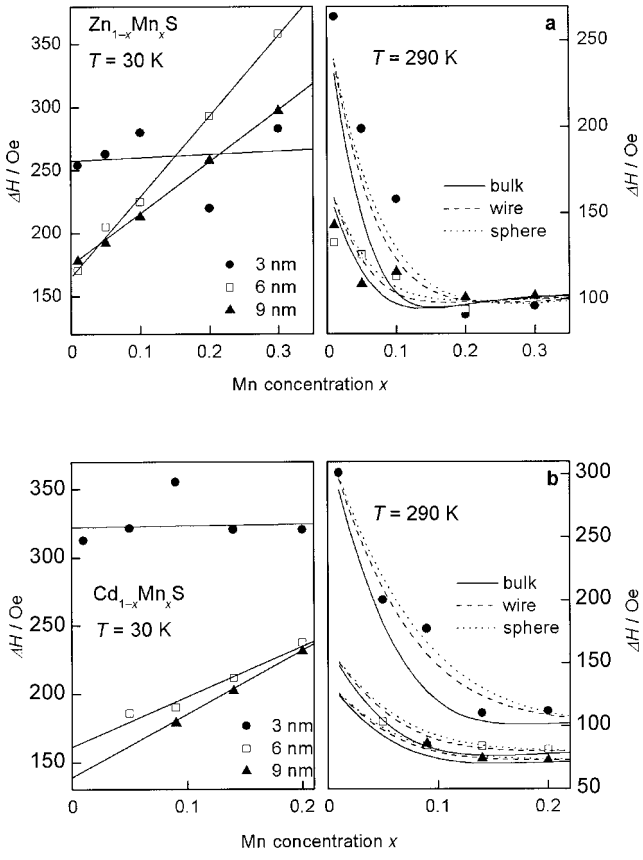

Figure 18. (a) Left: Plots of the EPR linewidth ΔH as a function of the doping level x at T = 30 K for $Zn_{1-x}Mn_xS$ nanoparticles with different diameters. The solid lines are linear fits. Right: Plots of the EPR linewidth ΔH as a function of of the doping level x at T = 290 K for $Zn_{1-x}Mn_xS$ nanoparticles with different diameters. The lines depict the results of model calculations described in the text. (b) corresponding graphs for and $Cd_{1-x}Mn_xS$ nanoparticles with different diameters.

tively by considering the effect of the nearest-neighbour interaction J_{nn}, which determines the linewidth behaviour at temperatures, where the Mn nearest-neighbour pairs are broken up. For this purpose, the Mn ions in the nanostructure can be divided up into two classes: (i) isolated Mn ions without manganese nearest neighbours and (ii) Mn ions with one or more nearest neighbours. Furthermore, as in the case of the discussion of the Curie–Weiss parameter Θ, the volume of the nanostructure will be divided into a volume close to the surface V^s_{nn} and a bulklike volume V^b_{nn} [see Equation (7)] and the discussion will be based on a zinc blende lattice for simplicity.

The probabilities for the occurrence of two classes of Mn ions as a function of x at the surface and in the bulk of the nanoparticles are given by Equation (10):

$$\begin{aligned} p^b_{is} &= (1-x)^{z^b_{nn}} & p^b_{nn} &= 1-p^b_{is} \\ p^s_{is} &= (1-x)^{z^s_{nn}} & p^s_{nn} &= 1-p^s_{is} \end{aligned} \tag{10}$$

The total linewidth as a function of x and diameter d is calculated according to Equation (11):

$$\Delta H(x,d) = \frac{V^b}{V}\sqrt{(\Delta H_{is}p^b_{is})^2 + (\Delta H^b_{nn}p^b_{nn})^2} + \frac{V^s}{V}\sqrt{(\Delta H_{is}p^s_{is})^2 + (\Delta H^s_{nn}p^s_{nn})^2} \tag{11}$$

It is assumed that in both volumes the linewidth contribution ΔH_{is} of the isolated manganese ions is well described by fits of the low temperature linewidth data according to Equation (9).

The linewidth contribution of the Mn ions with nearest neighbours is calculated in a similar fashion as in ref.[103] In both regions Equation (12) holds.

$$\Delta H_{nn} = \frac{H^2_{dip,nn} + H^2_{HF}}{H^i_{ex,nn}} \tag{12}$$

where $H_{dip,nn}$ is the mean dipolar exchange field for a Mn ion with at least one Mn nearest neighbour, which is approximated by Equation (13).

$$\left(H_{dip,nn}\right)^2 \approx \tfrac{3}{4}S(S+1)\mu_B{}^2 g^2\left[\frac{\gamma}{d^6_{nn}}\right] \tag{13}$$

for the surface as well as the bulk region. γ is basically a scaling factor for the square of the dipolar field due to one nearest neighbour Mn ion.

H_{HF} is the constant value for the hyperfine broadening determined at low T and $H^i_{ex,nn}$ is the isotropic nearest-neighbour exchange field. The latter is calculated according to Anderson and Weiss,[103] Equation (14):

$$H^i_{ex,nn} = 2.83\frac{J_{nn}}{g\mu_0\mu_B}\sqrt{S(S+1)} \tag{14}$$

For both (II,Mn)VI systems, γ is the only free parameter in this calculation and its value is determined by the linewidth limit at high x in the right graphs of Figure 18a and b.

The calculations were carried out for all nanoparticles. In each case, they were performed for bulk as well as for spherical and wirelike shapes. Again $a \approx 0.55$ nm and $a \approx 0.58$ nm were used for (Zn,Mn)S and (Cd,Mn)S, respectively. In the case of the Zn-based nanostructures, the best agreement was obtained for $\gamma = 0.9$ independent of the size of the nanostructure, while, for the Cd-based series, the best agreement was obtained for smaller values of γ, i.e. $\gamma = 0.6$ for the 6 and 9 nm nanostructures and $\gamma = 1$ for the 3 nm nanostructures. Assuming that the Mn–Mn nearest-neighbour distance d_{nn} is MnS-like, $a \approx 0.56$ nm for all Mn pairs, one obtains $\gamma = 1$ for (Zn,Mn)S nanostructures and $\gamma = 0.6$ and 0.5 for (Cd,Mn)S nanostructures. However, considering the crudeness of the model and the uncertainty in the Mn–Mn nearest-neighbour distance, the parameters obtained for γ are reasonable.

The theoretical curves for $Zn_{1-x}Mn_xS$ nanoparticles as well as for $Cd_{1-x}Mn_xS$ nanoparticles are also plotted in the right graphs of Figure 18b. Considering the overall agreement between theory and experiment, it appears better when a spherical shape of the magnetic nanoparticles is assumed. In particular, the linewidth decrease with increasing x is too rapid when a bulklike situation is considered. The corresponding slope is reduced by surface effects as the probability for Mn ions with manganese nearest neighbours is much lower in the surface region V^s_{nn} than in the bulklike volume V^b_{nn} for $0 < x < 0.2$.

In conclusion, changes in the macroscopic observables, e.g. the Curie–Weiss parameter Θ and the EPR linewidth ΔH of the paramagnetic phase of (II,Mn)VI nanoparticles with sizes below 10 nm due to reduced dimensions are observable. It appears that the microscopic coupling between the Mn ions (e. g. the nearest neighbour and next-nearest neighbour exchange constants J_{nn} and J_{nnn}) is not altered to a first approximation. The macroscopic modifications arise mainly due to geometrical restrictions, i.e. the number of neighbours in the various shells around a manganese ion in the surface region are considerably reduced compared to a manganese ion in the bulk of the structure. This effect becomes increasingly important with decreasing lateral dimensions of the nanostructure.

5. Conclusions

We have synthesised and thoroughly characterised (II,Mn)VI nanoparticles with Mn contents ranging from 0 to 0.3 incorporated inside mesoporous SiO_2 matrices with pore sizes of 3, 6, and 9 nm. By careful characterisation of the samples we demonstrate that under these synthesis conditions most of the Mn ions are incorporated on cation

sites of the II-VI host lattice and that the amount of Mn aggregated at the surface of the nanostructures is negligible. This allows us to thoroughly investigate the effects of reduced dimensionality on the magnetic and electronic properties of the (II,Mn)VI nanoparticles as a function of Mn content x and characteristic diameter d. Both, magnetic as well as electronic properties of the nanoparticles are modified due to the reduced lateral dimensions. We demonstrate by analysis of the EPR linewidth and EPR intensity that macroscopic magnetic properties such as the Curie–Weiss temperature are strongly affected by the reduction of the lateral dimensions whereas the microscopic coupling between the Mn ions (e.g. the exchange constants J_{nn} and J_{nnn}) is not altered to a first approximation. The macroscopic modifications arise mainly due to geometrical restrictions, i.e. the number of neighbours in the cation shells around a Mn ion in the surface region is considerably reduced compared to a Mn ion in the bulk. Due to the quantum confinement of the excitons in the nanostructures an increase of the direct band gap with decreasing particle size is observed. Furthermore, the band-gap bowing as a function of Mn content x is enhanced in the Cd compounds with decreasing nanostructure diameter d. This enhanced band-gap bowing can also be related to the alterations of the macroscopic magnetic properties [i.e. reduction of Curie–Weiss temperature $\Theta(x)$ and increase of effective Mn concentration x_{eff}], which occur due to the increase of the surface-to-volume ratio with decreasing nanostructure size.

Our work demonstrates that incorporating magnetic materials into mesoporous silica host matrices with adjustable, well-defined pore sizes in the range of 2 to 10 nm is an ideal approach for studying nanomagnetic phenomena as a function of particle size.

Acknowledgments

The authors would like to thank Günter Koch (Institute of Inorganic and Analytical Chemistry, Justus Liebig University Gießen) for the transmission electron micrographs. Financial support by the Deutsche Forschungsgemeinschaft (Fr, 1372/4-3 and He 2298/4-3) and the Fonds der Chemischen Industrie is gratefully acknowledged. This work was partially supported by the Bundesministerium für Bildung und Forschung (BMBF) under Contract No. 13N6917/0 (EKM) and by the Optodynamics Center of the Philipps-University.

[1] Y. Oka, J. X. Shen, K. Takabayashi, N. Takahashi, H. Mitsu, I. Souma, R. Pittini, *J. Lumin.* **1999**, *83–84*, 83.
[2] K. Takabayashi, N. Takahashi, I. Yagi, K. Yui, I. Souma, J. X. Shen, Y. Oka, *J. Lumin.* **2000**, *87–89*, 347.
[3] N. Takahashi, K. Takabayashi, I. Souma, J. Shen, Y. Oka, *J. Appl. Phys.* **2000**, *87*, 6469.
[4] A. A. Darhuber, H. Straub, S. O. Ferreira, W. Faschinger, H. Sitter, E. Koppensteiner, G. Brunthaler, G. Bauer, *Mater. Sci. Forum* **1995**, *182–184*, 423.
[5] A. Ribayrol, Y. S. Tang, H. P. Zhou, D. Coquillat, C. M. Sotomayor Torres, J. P. Lascaray, B. Lunn, D. E. Ashenford, G. Feuillet, J. Cibert, *J. Cryst. Growth* **1996**, *159*, 434.
[6] P. J. Klar, D. Wolverson, D. E. Ashenford, B. Lunn, T. Henning, *Semicond. Sci. Technol.* **1996**, *11*, 1863.
[7] P. J. Klar, D. Wolverson, J. J. Davies, W. Heimbrodt, M. Happ, T. Henning, *Phys. Rev. B* **1998**, *57*, 7114.
[8] G. Bacher, T. Kümmell, D. Eisert, A. Forchel, B. König, W. Ossau, C. R. Becker, G. Landwehr, *Appl. Phys. Lett.* **1999**, *75*, 956.
[9] G. Bacher, M. K. Welsch, A. McDonald, T. Kümmell, A. Forchel, B. König, C. Becker, W. Ossau, G. Landwehr, *Phys. Status Solidi A* **2000**, *178*, 359.
[10] S. Kuroda, Y. Terai, K. Takita, T. Okuno, Y. Masumoto, *J. Cryst. Growth* **1998**, *184–185*, 971.
[11] S. Kuroda, Y. Terai, K. Takita, T. Okuno, Y. Masumoto, *J. Cryst. Growth* **1998**, *184–185*, 274.
[12] Y. Terai, S. Kuroda, K. Takita, *Appl. Phys. Lett.* **2000**, *76*, 2400.
[13] Y. Terai, S. Kuroda, K. Takita, T. Takamasu, G. Kido, *J. Lumin.* **2000**, *87–89*, 396.
[14] S. Mackowski, S. Lee, J. K. Furdyna, M. Dobrowolska, G. Prechtl, W. Heiss, J. Kossut, G. Karczewski, *Phys. Status Solidi B* **2002**, *229*, 469.
[15] S. H. Xin, P. D. Wang, A. Yin, C. Kim, M. Dobrowolska, J. L. Merz, J. K. Furdyna, *Appl. Phys. Lett.* **1996**, *69*, 3884.
[16] M. Pinczolits, G. Springholz, G. Bauer, *Phys. Rev. B* **1999**, *60*, 11524.
[17] M. Pinczolits, V. Holy, P. Mayer, K. Wiesauer, T. Roch, G. Bauer, *Surf. Sci.* **2000**, *454–456*, 657.
[18] G. Springholz, M. Pinczolits, P. Mayer, V. Holy, G. Bauer, H. H. Kang, L. Salamanca-Riba, *Phys. Rev. Lett.* **2000**, *84*, 4669.
[19] L. Parthier, S. Luther, O. Portugall, M. von Ortenberg, K. Uchida, H. Kunimatsu, N. Miura, *J. Cryst. Growth* **1998**, *184–185*, 339.
[20] Z. H. Chen, M. C. Debnath, K. Shibata, T. Saitou, T. Sato, Y. Oka, *J. Appl. Phys.* **2001**, *89*, 6701.
[21] K. Yanata, Y. Oka, *Superlatt. Microstruct.* **1994**, *15*, 233.
[22] K. Yanata, K. Suzuki, Y. Oka, *J. Appl. Phys.* **1993**, *73*, 4596.
[23] K. Yanata, Y. Oka, *Jpn. J. Appl. Phys.* **1995**, *34*, 164.
[24] Y. Oka, K. Yanata, *J. Lumin.* **1996**, *70*, 35.
[25] Y. Wang, N. Herron, K. Moller, T. Bein, *Solid State Commun.* **1991**, *77*, 33.
[26] M. A. Chamarro, V. Voliotis, R. Grousson, P. Lavallard, T. Gacoin, G. Counio, J. P. Boilot, R. Cases, *J. Cryst. Growth* **1996**, *159*, 853.
[27] M. Morita, D. Rau, H. Fujii, Y. Minami, S. Murakami, M. Baba, M. Yoshita, H. Akiyama, *J. Lumin.* **2000**, *87–89*, 478.
[28] M. V. Artemyev, L. I. Gurinovich, A. P. Stupak, S. V. Gaponenko, *Phys. Status Solidi B* **2001**, *224*, 191.
[29] A. Henglein, *Ber. Bunsenges. Phys. Chem.* **1986**, *86*, 301.
[30] C. B. Murray, D. J. Norris, M. G. Bawendi, *J. Am. Chem. Soc.* **1993**, *115*, 8706.
[31] C. Petit, P. Lixon, M. P. Pileni, *J. Phys. Chem.* **1990**, *94*, 1598.
[32] C. Petit, T. K. Jain, F. Billoudet, M. P. Pileni, *Langmuir* **1994**, *10*, 4446.
[33] L. Motte, C. Petit, L. Boulanger, P. Lixon, M. P. Pileni, *Langmuir* **1992**, *8*, 1049.
[34] H. Sato, T. Hirai, I. Komasawa, *Ind. Eng. Chem. Res.* **1995**, *34*, 2493.
[35] J. Tanori, N. Duxin, C. Petit, P. Veillet, M. P. Pileni, *Colloid Polym. Sci.* **1995**, *273*, 886.
[36] J. Cizeron, M. P. Pileni, *J. Phys. Chem.* **1995**, *99*, 17410.
[37] J. Cizeron, M. P. Pileni, *J. Phys. Chem. B* **1997**, *101*, 8887.
[38] S. K. Haram, A. R. Mahadeshwar, S. G. Dixit, *J. Phys. Chem.* **1996**, *100*, 5868.
[39] M. P. Pileni, *Langmuir* **1997**, *13*, 3266.
[40] M. L. Curri, A. Agostiano, L. Manna, M. D. Monica, M. Catalano, L. Chiavarone, V. Spagnolo, M. Lugara, *J. Phys. Chem. B* **2000**, *104*, 8391.
[41] K. Moller, T. Bein, *Chem. Mater.* **1998**, *10*, 2950.
[42] M. P. Pileni, *Cryst. Res. Technol.* **1998**, *33*, 1155.
[43] R. Köhn, M. Fröba, *Catal. Today* **2001**, *68*, 227.
[44] J. S. Beck, J. C. Vartuli, W. J. Roth, M. E. Leonowicz, C. T. Kresge, K. D. Schmitt, C. T.-W. Chu, D. H. Olson, E. W. Shep-

pard, S. B. McCullen, J. B. Higgins, J. L. Schlenker, *J. Am. Chem. Soc.* **1992**, *114*, 10834.
[45] M. Thommes, R. Köhn, M. Fröba, *J. Phys. Chem. B* **2000**, *104*, 7932.
[46] D. Zhao, J. Feng, Q. Huo, N. Melosh, G. H. Fredrickson, B. F. Chmelka, G. D. Stucky, *Science* **1998**, *279*, 548.
[47] J. D. Holmes, D. M. Lyons, K. J. Ziegler, *Chem. Eur. J.* **2003**, *9*, 2144.
[48] L. E. Brus, *J. Chem. Phys.* **1984**, *80*, 4403.
[49] L. E. Nair, S. Sinha, K. C. Rustagi, *Phys. Rev. B* **1987**, *35*, 4098.
[50] A. Henglein, *Chem. Rev.* **1989**, *89*, 1861.
[51] P. E. Lippens, M. Lannoo, *Phys. Rev. B* **1989**, *39*, 10935.
[52] Y. Wang, N. Herron, *Phys. Rev. B* **1990**, *42*, 7253.
[53] T. Vossmeyer, L. Katsikas, M. Giersig, I. G. Popovic, K. Diesner, A. Chemseddine, A. Eychmüller, H. Weller, *J. Phys. Chem.* **1994**, *98*, 7665.
[54] A. P. Alivisatos, *J. Phys. Chem.* **1996**, *100*, 13226.
[55] A. C. Gossard, S. Fafard, *Solid State Commun.* **1994**, *92*, 63.
[56] G. W. Bryant, *J. Lumin.* **1996**, *70*, 108.
[57] R. Nötzel, *Semicond. Sci. Technol.* **1996**, *11*, 1365.
[58] A. Ekimov, *J. Lumin.* **1996**, *70*, 1.
[59] G. A. Prinz, *Science* **1998**, *282*, 1660.
[60] R. N. Bhargava, D. Gallagher, X. Hong, A. V. Nurmikko, *Phys. Rev. Lett.* **1994**, *72*, 416.
[61] A. A. Bol, A. Meijerink, *Phys. Rev. B* **1998**, *58*, R15997.
[62] A. A. Bol, A. Meijerink, *J. Lumin.* **2000**, *87–89*, 315.
[63] D. J. Norris, N. Yao, F. T. Charnock, T. A. Kennedy, *Nanoletters* **2001**, *1*, 3.
[64] M. A. Hines, P. Guyot-Sionnest, *J. Phys. Chem. B* **1998**, *102*, 3655.
[65] L. Levy, J. F. Hochepied, M. P. Pileni, *J. Phys. Chem.* **1996**, *100*, 18322.
[66] L. Levy, N. Feltin, D. Ingert, M. P. Pileni, *J. Phys. Chem. B* **1997**, *101*, 9153.
[67] F. J. Brieler, M. Fröba, L. Chen, P. J. Klar, W. Heimbrodt, H.-A. Krug von Nidda, A. Loidl, *Chem. Eur. J.* **2002**, *8*, 185.
[68] L. Chen, H. Falk, P. J. Klar, W. Heimbrodt, F. Brieler, M. Fröba, H.-A. Krug von Nidda, A. Loidl, Z. Chen, Y. Oka, *Phys. Status Solidi B* **2002**, *229*, 31.
[69] A. V. Kouzema, M. Fröba, L. Chen, P. J. Klar, W. Heimbrodt, *Adv. Funct. Mater.* **2005**, *15*, 168.
[70] F. J. Brieler, P. Grundmann, M. Fröba, L. Chen, P. J. Klar, W. Heimbrodt, H.-A. Krug von Nidda, T. Kurz, A. Loidl, *J. Am. Chem. Soc.* **2004**, *126*, 797.
[71] N. Feltin, L. Levy, D. Ingert, M. P. Pileni, *Adv. Mater.* **1999**, *11*, 398.
[72] M. P. Pileni, *Catal. Today* **2000**, *58*, 151.
[73] L. Chen, P. J. Klar, W. Heimbrodt, F. Brieler, M. Fröba, H.-A. Krug von Nidda, T. Kurz, A. Loidl, *J. Appl. Phys.* **2003**, *93*, 1326.
[74] Y. Tanabe, S. Sugano, *J. Phys. Soc. Jpn.* **1954**, *9*, 753.
[75] A. Twardowski, P. Swiderski, M. von Ortenberg, R. Pauthenet, *Solid State Commun.* **1984**, *50*, 509.
[76] A. Twardowski, T. Dietl, M. Demianiuk, *Solid State Commun.* **1983**, *48*, 845.
[77] C. T. Tsai, S. H. Chen, D. S. Chuu, W. C. Chou, *Phys. Rev. B* **1996**, *33*, 8207.
[78] M. Ikeda, K. Itoh, H. Sato, *J. Phys. Soc. Jpn.* **1968**, *25*, 455.
[79] R. B. Bylsma, W. M. Becker, J. Kossut, U. Debska, *Phys. Rev. B* **1986**, *33*, 8207.
[80] B. E. Larson, K. C. Hass, H. Ehrenreich, A. E. Carlson, *Phys. Rev. B* **1988**, *37*, 4137.
[81] M. Taniguchi, M. Fujimori, M. Fujisawa, T. Mori, I. Souma, Y. Oka, *Solid State Commun.* **1987**, *62*, 431.
[82] R. Weidemann, H.-E. Gumlich, M. Kupsch, H.-U. Middelmann, U. Becker, *Phys. Rev. B* **1992**, *45*, 1172.
[83] Y.R. Lee, A. K. Ramdas, R. L. Aggarwal *Proc. 18th Int. Conf. on Physics of Semiconductors* **1986**, World Scientific.
[84] D. Theis, *Phys. Lett. A* **1976**, *59*, 154.
[85] R. R. Galazka, S. Nagata, P. H. Keesom, *Phys. Rev. B* **1980**, *22*, 3344.
[86] M. A. Novak, O. G. Symko, D. J. Zheng, S. Oseroff, *Phys. Rev. B* **1986**, *33*, 6391.
[87] N. Samarth, J. K. Furdyna, *Phys. Rev. B* **1988**, *37*, 9227.
[88] J. Schneider, S. R. Sircar, A. Z. Räuber, *Z. Naturforsch. A* **1963**, *18*, 980.
[89] J. Lambe, C. Kikuchi, *Phys. Rev. B* **1960**, *119*, 1256.
[90] Y. J. Ishikawa, *J. Phys. Soc. Jpn.* **1966**, *21*, 1473.
[91] F. J. Brieler, P. Grundmann, M. Fröba, L. Chen, P. J. Klar, W. Heimbrodt, H.-A. Krug von Nidda, T. Kurz, A. Loidl, *Chem. Mater.* **2005**, *17*, 795.
[92] P. H. Borse, D. Srinivas, R. F. Shinde, S. K. Date, W. Vogel, S. K. Kulkarni, *Phys. Rev. B* **1999**, *60*, 8659.
[93] J. K. Furdyna, N. Samarth, R. B. Frankel, J. Spalek, *Phys. Rev. B* **1988**, *37*, 3707.
[94] C. Chen, M. Qu, W. Hu, X. Zhang, F. Lin, H. Hu, K. Ma, W. Giriat, *J. Appl. Phys.* **1991**, *69*, 6114.
[95] Y. Q. Yang, P. H. Keesom, J. K. Furdyna, W. Giriat, *J. Sold State Chem.* **1983**, *49*, 20.
[96] Y. Shapira, S. Foner, D. Heiman, P. A. Wolff, C. R. McIntyre, *Solid State Commun.* **1989**, *71*, 355.
[97] Landolt-Börnstein, Numerical Data and Functional Relationships in Science and Technology, Vol. 17b, Springer, Berlin **1982**.
[98] R. E. Kremer, J. K. Furdyna, *Phys. Rev. B* **1985**, *31*, 1.
[99] S. B. Oseroff, *Phys. Rev. B* **1982**, *25*, 6584.
[100] H. A. Sayad, S. M. Bhagat, *Phys. Rev. B* **1985**, *31*, 591.
[101] S. B. Oseroff, R. Calvo, Z. Fisk, F. Acker, *Phys. Lett. A* **1980**, *80*, 311.
[102] J. H. van Vleck, *Phys. Rev.* **1948**, *74*, 1168.
[103] P. W. Anderson, P. R. Weiss, *Rev. Mod. Phys.* **1953**, *25*, 269.

Received: April 26, 2005
Published Online: August 17, 2005

